aerospace

MDPI

Article

Visualization of the Detonation Wave Structure in a Small-Scale Hydrogen–Oxygen Rotating Detonation Combustor [†]

Wolfgang Armbruster [1,*], Ewen Bard [1,2], Michael Börner [1], Kilian Rheindorf [1], Jan Martin[1], Leon Lober [1], Stephan General [1] and Justin S. Hardi [1]

[1] Institute of Space Propulsion, German Aerospace Center (DLR), 74239 Lampoldshausen, Germany; michael.boerner@dlr.de (M.B.); justin.hardi@dlr.de (J.S.H.)

[2] DMPE (Multi-Physics Department for Energetics), ONERA, Universite Paris Saclay, F-91123 Palaiseau, France

* Correspondence: wolfgang.armbruster@dlr.de

[†] This paper is an extended version of our paper published in Armbruster, W.; Bard, E.; Börner, M.; Rheindorf, K.; Lober, L.; General, S.; Hardi, J. Visualization of the Detonation Wave Structure in a Small-Scale Hydrogen-Oxygen Rotating Detonation Combustor. In Proceedings of the 35th International Symposium on Space Technology and Science (ISTS), Tokushima, Japan, 12–18 July 2025.

Abstract

This study presents the high-speed visualization of the detonation wave structure in a small-scale hydrogen–oxygen rotating detonation combustor. A 68 mm Rotating Detonation Combustor was modified with a quartz-glass ring, such that radial optical access into the annular detonation chamber was realized. The optical access window covers approximately the first 22 mm of the detonation chamber. The modified experiment was hot-fire tested with the propellant combination gaseous hydrogen–oxygen. Simultaneous high-speed imaging from the back-end of the chamber and normal to the chamber axis allows a thorough investigation of the detonation wave characteristics. Both high-speed cameras were operated at 180,000 frames per second in order to resolve and capture the detonation waves. The downstream camera was used in order to investigate the number of waves and the spinning direction. A stable regime of three co-rotating waves was observed. The wave speed achieved 71% of the theoretical CJ-velocity. The second camera recorded the passing detonation waves through a quartz ring via OH* emissions. From the post-processed OH* images, a better understanding of the detonation wave structure, including the filling height of the fresh gas mixture as well as the approximate angles of the detonation and the shock wave, could be gained. The obtained height of the detonation wave is about 11–12 mm or 6–7 detonation cell sizes for the given setup and experimental conditions.

Keywords: rotating detonation engine; pressure gain combustion; hydrogen–oxygen; detonation wave structure; rocket engine

Check for updates

Academic Editor: Bo Zhang

Received: 20 November 2025

Revised: 3 February 2026

Accepted: 5 February 2026

Published: 7 February 2026

1. Introduction

Detonative propulsion systems have the potential to significantly increase the specific impulse of rocket engines. The values for the increase in specific impulse that can be found in literature are up to about 20% [1] depending on the propellant combination and the application case. The most prominent solutions to realize detonative propulsion are Pulsed Detonation Engines (PDEs) and Rotating Detonation Engines (RDEs) [1–3].

The basic principle of the detonation wave process inside a rotating detonation combustor (RDC) has been known for decades [4–6] and is presented in Figure 1 for an annular chamber with length L_c, outer diameter d_c. The mixture is injected (1) from the aft end

https://doi.org/10.3390/aerospace13020158

of the chamber (2) such that a rotating detonation front (3), spaced by a spatial distance l between two consecutive detonation waves, combusts the fresh mixture (4) that has reached a certain fill height h. An oblique shock (5) is produced by the detonation wave, and the combustion products exit through the open end of the chamber (6).

Apart from the theoretical efficiency increase [1,2], additional advantages of rotating detonation rocket engines are a lower feed-pressure to achieve similar performance, which could reduce turbopump powers [7] and most importantly compactness of the engine [1], due to the constant volume combustion.

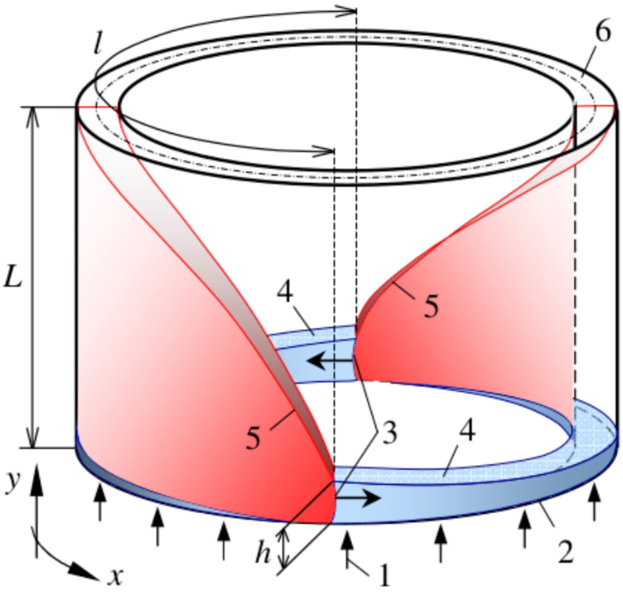

Figure 1. Schematic of the working principle of an RDE, adapted from [8]. 1—propellant injection; 2—injection plane; 3—detonation front; 4—fresh propellant layer; 5—oblique shock; 6—exit plane.

For about 15 years, there has been a rapidly growing interest in RDE technology worldwide for the given advantages of pressure gain combustion [3]. In general, compared to the more commonly used propellant combinations of O_2-CH_4 for rocket-type RDEs [3,9–16] or air-breathing RDE-research with hydrogen [3,17,18], the studies on hydrogen–oxygen RDCs are rather limited [5,19–21]. This could be attributed to the fast chemical reactions for hydrogen–oxygen, even for deflagration [22]. So, in an RDC environment, it is challenging to reduce the deflagration losses with this propellant combination. Nevertheless, there are still a few examples that prove that achieving detonation waves in Rotating Detonation Combustors is possible with hydrogen–oxygen [5,19–21,23].

The high repetition rate of the detonation waves in RDCs presents a challenge for the diagnostics for the investigation of the rotating detonation waves. One common technique to study and characterize the detonation wave regime is to install a powerful high-speed camera downstream of the annular detonation chamber and visualize the number and the direction of the waves [11,17,21,24]. This diagnostic technique is therefore really useful to identify the number of waves and thus the speed of the rotating wave in the annular detonation chamber. For that reason, putting a high-speed camera downstream of the RDC to visualize the detonation waves can be considered almost as a standard practice in RDC testing and has also already applied to hydrogen–oxygen RDCs [21,25].

Another challenge is that, until today, there exist no generally applicable design guidelines for RDC detonation chambers and injectors that ensure stable detonation waves. While the groundbreaking work from Bykovskii et al. [6] laid the foundation for design guidelines for the RDC chamber dimensions, many studies now focus on the injector design, which is crucial for stable detonation waves. In order to achieve stable and strong detonation waves, the injectors need to be able to inject and achieve good mixing of the fresh propellants before the next detonation wave arrives. Due to the high repetition rate of several Kilohertz in RDEs, the time window for injection and mixing is typically in the order of less than 100 µs.

A simple scaling law for RDCs and their injectors is based on the so-called filling height of the fresh gases, which are consumed by the rotating detonation wave [2,6]. This parameter can define how many waves could appear, how to dimension the RDC chamber, and thus also has an influence on the injector design [1]. However, measuring this crucial parameter h is not a trivial experiment and thus the available information is rather limited. For different propellant combinations, Bykovskii et al. [6] published the well-known semi-empirical correlation $h \approx (12 \pm 5)\lambda$ to estimate h in function of the detonation cell size λ. However, it is evident that the uncertainty in the given equation is high, and a more detailed knowledge of h is necessary to design RDCs and RDC injectors. One method to gain knowledge on the detonation wave structure, including the detonation wave height and the angle of the detonation wave and the trailing shock wave, is to equip the combustor with a large number of high-frequency pressure sensors and based on the time and phase angle of the pressure oscillations at different locations inside the combustor interpolate the important wave structures [26]. Another possibility to experimentally investigate the detonation wave structure and the interaction with mixing is to radially visualize the detonation waves inside the annular detonation chambers [9,14,18,20,27–33]. This has already been demonstrated for air-breathing RDCs [28,30,33] as well as rocket-type RDCs [9,14,20,27,29,31,32]. Due to the increased temperatures in rocket RDCs, realizing optical access in the detonation chamber is a challenge.

While there are a few examples of successful detonative operation of hydrogen–oxygen RDCs with the visualization of the detonation waves from downstream of the chamber axis, to the authors' knowledge, there has been only one attempt to radially visualize the detonation wave front structure of a O_2/H_2 detonation wave inside an RDC [20]. However, the visualization quality of the detonation waves in the study from Bykovskii et al. [20] is not comparable with modern studies, and in addition, the study also does not contain many details regarding the design of the experiment, such as the injector design and scale, the optical access window design and a proper scaling for the visualized waves. For the given reasons, to the authors' knowledge, there is also a lack of a well-documented hydrogen–oxygen RDC test case with a radial wave visualization for the validation of numerical tools. Since it was shown in RDCs using different propellant combinations that the radial visualization of the detonation wave front is highly valuable in understanding the mixing processes and the filling height, which is important to improve injector designs, it is the goal of this study to visualize the structure of the detonation wave and a hydrogen–oxygen RDC. In order to do so, the existing and already studied small-scale 68 mm RDC at DLR Lampoldshausen was modified to achieve radial optical access [22].

2. Experimental Methods

This chapter describes the experimental setup for the visualization of the detonation wave structure as well as the methodology to derive the results from the experimental data.

2.1. Test Bench M3.1

The initial RDC run-in tests were conducted at the M3 test field at DLR Lampoldshausen [34]. While this test bench offers great flexibility and cost-effective testing, the propellant flow rates are limited. The M3 test field currently houses three active test positions (M3.1, M3.3, M3.5) for tests with cryogenic media liquid or gaseous oxygen and gaseous hydrogen or hydrocarbon fuels on a laboratory scale and feed-line pressures of up to 40 bar [35]. The test bench M3.1 is designed for injection, ignition and combustion testing. Test sequences can be varied by fast-reacting valves that allow a sequencing of the fuel and oxidizer flow rate in the order of milliseconds with a reproducibility in the order of 5 ms for gaseous media. The temperature range for GH_2 is 200 K to ambient. Maximum mass flow rates are in the order of 70 g/s depending on the mixture ratio and the test set-up [35]. For the studied RDC tests, both oxygen and hydrogen are fed in a gaseous state at approximately ambient temperatures.

2.2. Small-Scale Hydrogen–Oxygen RDC at DLR

The general setup of the existing RDC at DLR, without optical access as shown in Figure 2, has already been described in previous publications [24,25]. The RDC hardware was designed to be highly modular and different variations have already been tested [36,37]. For that reason, only a short summary of the main features of the general RDC design is presented here and the main focus of the experimental setup description is set on the optical access and the optical diagnostics.

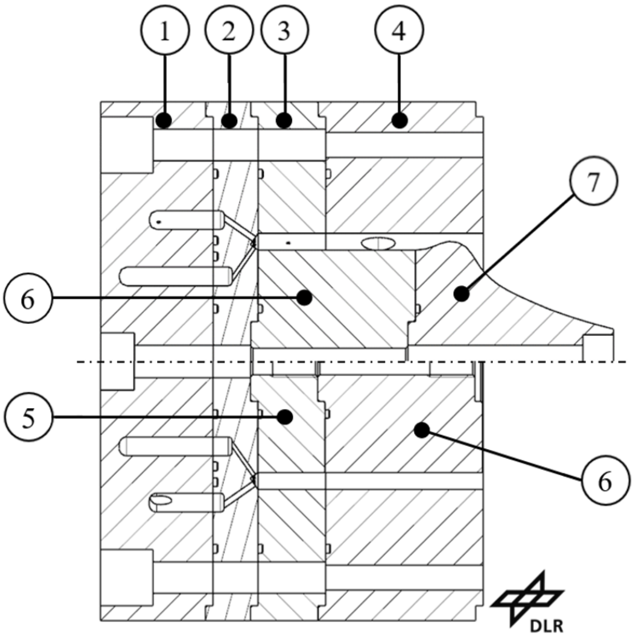

Figure 2. Original DLR RDC without optical access of previous studies [24]. The top half shows the configuration with a throat and an aerospike nozzle. Bottom half of the annular chamber configuration without constriction. (1) Manifold plate, (2) Injector plate, (3) Measurement ring, (4) Ignition ring, (5) Core cylinder, short, (6) Core cylinder, long, (7) Aerospike nozzle.

2.2.1. Chamber Design

The DLR RDC was designed for the propellant combination hydrogen–oxygen, and to be operated at the research test bed M3. Due to the limited mass flow rates at this test bench, a relatively small RDC was realized, and a simple and robust uncooled heat-sink design was chosen. The detonation chamber segments and injector plate are made from a copper alloy (CuCr1Zr), while the injector manifold is made from stainless steel. The outer diameter of the annular chamber is 68 mm. As was described before, an important aspect of the experimental design was modularity. For that reason, already different injector plates, center body pieces and measurement rings exist. In the standard configuration, which is presented in Figure 2, the RDC chamber had a length of about 50 mm and an inner diameter of 59 mm, yielding a channel width of 4.5 mm. However, also different channel widths and even hollow-core settings have been tested recently [36].

In the previously conducted tests, it was observed that for the given RDC configuration, an increased channel width resulted in more stable co-rotating waves, even though this further reduces the chamber mass flux. For that reason, it was decided to test the optically accessible RDC with a gap width of 10 mm, yielding an inner diameter of 48 mm [22]. To include the optical access window, the length of the outer body of the chamber increased slightly to 66 mm. The length of the inner or center body was 42 mm and thus the inner body was recessed with respect to the outer chamber wall. As can be seen in Figure 2, the RDC can be tested with and without a throat and a nozzle. For better visualization of the wave dynamics through a downstream camera and in order to reduce the loads on the window, no nozzle was installed in this study. A sketch of the modified RDC configuration with optical access used in this study, with the most important dimensions of the detonation chamber, is presented in Figure 3.

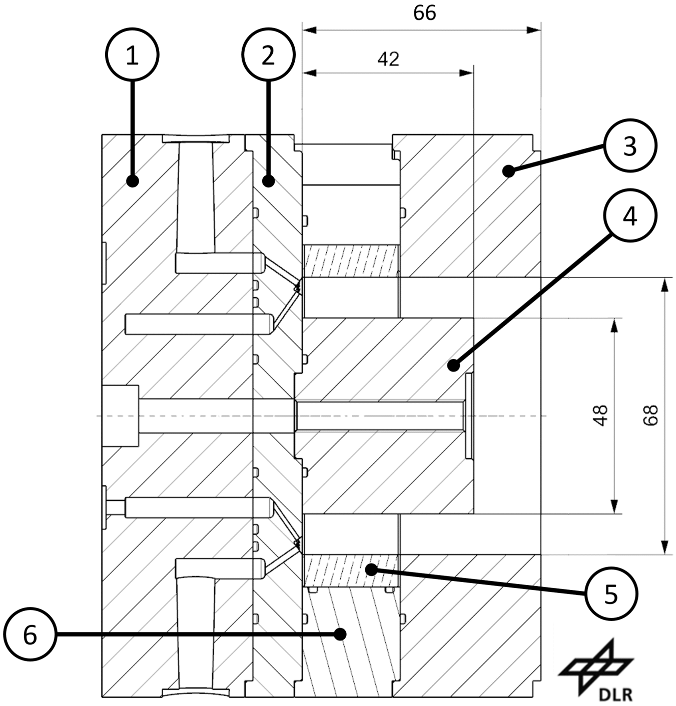

Figure 3. Sketch of the modified DLR RDC with optical access used in this study. (1) Manifold plate, (2) Injector plate, (3) Outer body "Detonation Ring" (4) Center Body, (5) Optical access quartz ring (6) PTFE ring to center and seal the quartz ring.

2.2.2. Injector Design

The injector plate consists of 72 pairs of unlike doublet impinging jets to supply the gaseous propellants from the two manifold rings into the annular detonation chamber. The O_2 injectors have a diameter of 1.5 mm and the H_2 injectors a diameter of 1.0 mm, respectively. In order to balance the momentum and also the large difference in injection velocities between hydrogen and oxygen, the two injector holes are tilted with respect to the chamber axis, resulting in uneven angles of 35° for oxygen and 55° for hydrogen, respectively. Since the injector plate was designed for the RDC chamber configuration of 68 mm outer diameter and a channel gap width of 4.5 mm, there is a zone on the injection plate towards the inner body, where no propellants are injected in the configuration of the increased channel width of 10 mm.

2.2.3. Ignition Method

In the first run-in tests of the RDC at DLR, the chamber was ignited with an automotive spark plug installed directly in the chamber wall [34]. For most of the conducted RDC tests, the hardware was updated, such that a hydrogen–oxygen pre-detonator was installed and successfully initiated the RDC operation [24,38]. However, since the pre-detonator produces the strongest detonation wave inside the RDC with peak pressures sometimes exceeding 20 bar, it was decided to switch back to a direct ignition with the spark plug for the optically accessible RDC tests again. This is deemed acceptable because spinning waves were also observed in the tests with the spark plug ignition [34]. By doing so, the ignition process of the RDC should be less harsh for the window.

2.2.4. Optical Access

Generally, in RDCs, it is expected that the detonation waves propagate in close vicinity to the injector plate [2,3,6]. This was also observed in other RDCs with optical access [9,10,14,18,27,28,30]. For that reason, it was decided for an easy realization of optical access close to the injection plane, to replace the first segment of the outer body of the existing RDC, the so-called "measurement ring" (see also Figure 2) by a quartz-glass ring.

The resulting quartz ring is made from HOQ310 (Heraeus, Hanau, Germany) and is 23 mm long. The HOQ310 material was chosen since it has comparable transmission at the OH* wavelengths peaking at 306–310 nm, but at the same time reduced cost compared to higher quality quartz material, such as Suprasil. Graphite seals with a thickness of 0.5 mm are placed between the quartz ring and the metal components, injector plate and detonation ring, respectively. The quartz ring has the same inner diameter as the RDC outer body (68 mm) and an outer diameter of 84 mm, resulting in a wall thickness of 8 mm. This was chosen as a compromise between sufficient wall thickness to withstand the mechanical loads, but at the same time not being too thick to be less prone to thermal shock. Due to the relatively thin quartz ring and a viewing angle that is mostly normal to the window, the distortion of the quartz ring is neglected in this study. Instead, based on the dimensions of the optical access field of view, a constant millimeter-to-pixel conversion is applied in the radial and axial directions individually. Furthermore, for centering purposes, a small step in the copper-alloy detonation ring, which is mounted downstream of the optical access, covers the last 1.5 mm of the quartz ring. Thus, the first 0.5 to 22 mm of the RDC are optically accessible. With respect to the well-known semi-empirical relation from Bykovskii et al. [6] for the filling height $h = (12 \pm 5)\lambda$ and with $\lambda \approx 1.3$ mm for hydrogen–oxygen at stoichiometric conditions [16,39,40], this length should cover the location of the passing detonation waves sufficiently. Furthermore, an investigation of the heat flux distribution in this DLR RDC [37] also showed the highest heat flux to be located in the first $\approx$10 mm from the faceplate, which gives another indication that the optical access window should cover the region of the detonation waves.

Since the high-speed camera can only record the wave dynamics from one radial position with a limited spatial resolution due to the high frame rate, an outer ring made from PTFE was built that holds the quartz ring in place and also supports the sealing concept of the setup. This outer PTFE ring has a cut-out space with a width of 32 mm. For the annular detonation chamber, this yields an observable angle of about 31°.

A cut through the CAD assembly of the optically accessible RDC is shown in Figure 3. The final assembly mounted on the thrust frame of the M3.1 test bench can be seen in Figure 4. Here, the PTFE ring for centering and sealing of the optical access quartz ring can clearly be observed. Also, in Figure 4, an end cap is installed in order to perform leakage tests before the first hot-fire testing, which is removed for the actual RDC tests.

Furthermore, since the so-called "measurement ring" of the original RDC was replaced by the quartz ring, there are no high-frequency pressure sensors installed in the optical access configuration of the RDC. For that reason, the characterization of the detonation wave regime has to be solely based on the downstream high-speed camera data.

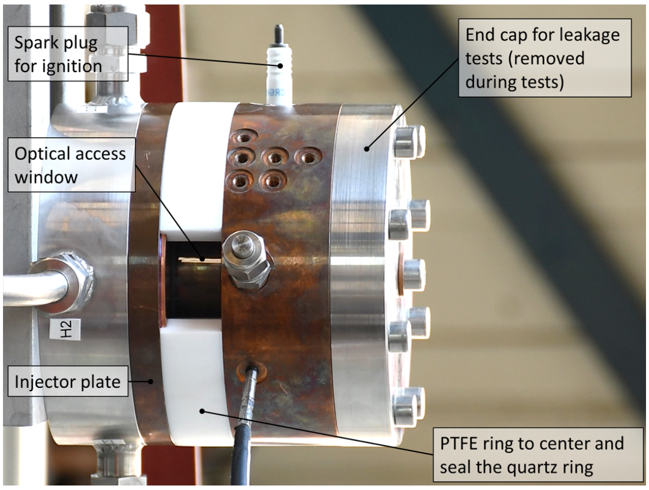

Figure 4. DLR RDC setup with optical access window before testing. Modified from [22].

2.3. Measurements

In order to characterize the operating condition of the RDC, both the test bench and the RDC are equipped with conventional, low-frequency diagnostics. The propellant mass flow rates, which are fed from the test bench to the RDC manifold are measured with high-precision Coriolis flowmeters.

The propellant manifolds of the RDC are both equipped with static pressure sensors (Kistler type 4043A, Kistler, Winterthur, Switzerland) and type K thermocouples. The Kistler sensors are sampled at 10 kHz, the thermocouples with 1 kHz, and the Coriolis with 100 Hz, respectively. Due to the replacement of the previously used measurement ring in this RDC with the optical access quartz ring, there were no chamber pressure sensors (both high-frequency pressure oscillations and average chamber pressure) in this study.

Since the Coriolis are installed far upstream in the feed system of the M3 test bench and have a low sampling rate, an estimation of the mass flow rate with a better time resolution was calculated based on the manifold pressures and discharge coefficient for the injector, which is calculated during steady-state mass flow rate regimes and the mass flow rate measurements of the Coriolis flowmeters. A more detailed description of this procedure can be found in [36].

Table 1 summarizes the calculated measurement uncertainties of the conventional diagnostics to describe the time-averaged operating condition of the RDC.

Table 1. Measurement uncertainties in this study.

Physical Value	Sensor or Calculation	Uncertainty
Propellant flow rate [kg/s]	Coriolis flowmeter	0.1%
Propellant temperature [K]	Type K thermocouple	±1.5 K
Manifold pressure [bar]	Kistler 4043A	1%
Transient flow rate [kg/s]	c_D-value and injector pressure drop	<2.5%
Propellant mixture ratio [-]	ROF = $\dot{m}_{O2}/\dot{m}_{H2}$	<3.5%

The uncertainty on ROF translates into an uncertainty of the evaluated CJ speed DCJ less than 2%, assuming the mixture in front of the detonation is perfectly homogeneous and corresponds to the injected composition.

2.4. Operating Conditions in This Study

The described RDC experiment and its components have already been tested more than 100 times. The mass flow rates have been varied from 15 g/s–70 g/s at the test bench M3.1 and up to 300 g/s at the test bench M11 [25,36].

To reduce thermal and mechanical loads on the quartz window, the RDC tests with optical access were performed with an intermediate mass flow rate of $\dot{m} \approx 50$ g/s and a test time of <1 s. As was described before, a configuration with a larger gap width of 10 mm was installed with the optical access windows. This yields a rather low detonation chamber mass flux of $g = \dot{m}/A_c \approx 27$ kg/m²/s. Compared to other rocket-type RDE experiments in literature [3,6,14,21,23,27] this puts the operating conditions at the lower end of the reasonable mass fluxes for RDC operability. However, in previous tests, it was observed that rotating waves were present at comparable mass flow rates.

In total, three tests have been realized with the optical access ring. However, due to the complexity of the optical diagnostics setup, the optical data of the first test run was considered as not satisfactory for analysis. This leaves two test runs for the investigation of the detonation wave structure. To also understand the reproducibility of the wave structure, it was aimed to perform these two tests with the same feeding mass flow rates of the propellants. In the third and last test, the oxygen mass flow rate was slightly lower, resulting still in similar conditions with a reduced oxidizer to fuel ratio ROF $= \dot{m}_{O_2}/\dot{m}_{H_2}$ or increased equivalence ratio ϕ.

Figure 5 shows the manifold pressures for both oxygen and hydrogen during one of the performed test runs. As can be seen, a constant feed pressure is rapidly established and steady-state propellant feeding conditions are achieved between 200 ms and 600 ms, when the oxygen flow rate is steadily reduced before the shutdown of the RDC. The short test duration is chosen based on the heat-sink design of the experiment. However, due to the typical detonation wave speeds, this test duration is still sufficient to observe several thousand rotations of the waves. Due to the replacement of the measurement ring with the quartz ring, there was no measurement of both the averaged, static chamber pressure and the high-frequency pressure oscillations during the studied RDC tests with optical access. However, based on the experience of previous tests with this RDC, including pressure measurements [25], the mean chamber pressure for these conditions is about 1 bar.

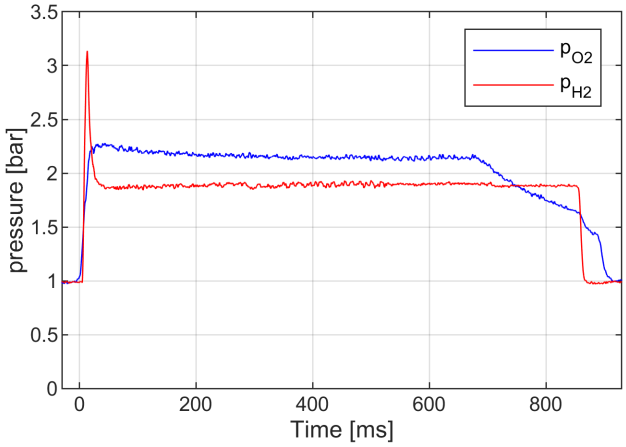

Figure 5. Propellant manifold pressure for one of the test runs with optical access [22].

As will be shown later, a stable co-rotating detonation wave regime was observed during this steady state condition. This was a repeatable behavior in both analyzed test runs. For that reason, the operating conditions are averaged over the steady-state time window of interest. Table 2 summarizes the tested and analyzed load points with the optical access quartz ring for which both steady injection conditions and a stable detonation wave regime were observed. The presented theoretical wave velocities (u_{CJ}) were calculated using NASA CEA [41] with an ambient temperature of the fresh gas mixture, the presented ROF and a pressure of 1 bar in front of the detonation wave.

Table 2. Operating conditions of the two analyzed RDC test runs with optical access.

Test No.	$\dot{m}_{tot}$	ROF (ϕ)	u_{CJ}
#2	50 g/s	10.5 (0.76)	2620 m/s
#3	48.5 g/s	9.5 (0.84)	2695 m/s

2.5. Optical Diagnostics

Two Photron high-speed cameras were used in the underlying tests. In order to visualize and analyze the detonation wave dynamics, one high-speed camera was placed downstream of the RDC exit, similar to previous RDC tests at DLR [24,25]. Here, the Photron SA-Z (Photron, Tokyo, Japan) was placed aligned with the chamber axis and at a distance of about 7 m away from the RDC. No special emission filter was used for this camera. A lens with a 500 mm focal length and an aperture of 4.5 was used. The spatial resolution was 256 × 256 pixels and the outer diameter of the annular RDC was covered by about 210 × 210 pixels.

A second high-speed camera, the Photron SA-X2, was placed normal to the chamber axis to visualize the passing detonation waves through the optical access window. Both cameras were synchronized at 180,000 frames per second (FPS). The resolution was set to 256 × 168 pixels, with about 120 × 80 pixels covering the optical access into the annular RDC chamber. In order to capture OH* emissions from the detonation wave, the SA-X2 camera was combined with a Hamamatsu image intensifier (type C10880) (Hamamatsu, Shizuoka, Japan). A special UV-lens with 105 mm focal length and an aperture of 4.5 was installed and an OH* filter with 310 ± 5 nm was mounted on the lens. This camera was installed with a radial distance of about 1.5 m from the RDC. The simplified setup of the experiment and the optical diagnostics is presented in Figure 6.

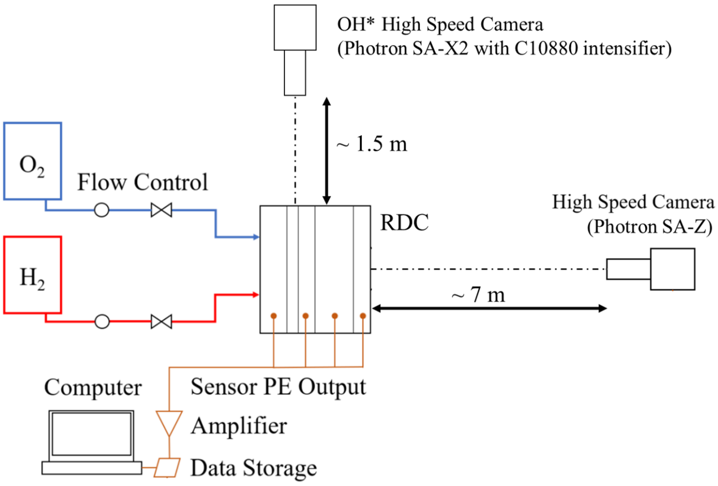

Figure 6. Sketch of the experimental with the RDC and the optical diagnostics as seen from the top [22].

2.6. Image Processing Routine

The Photron high-speed cameras both record the images in gray scale. In order to better visualize the waves and to investigate both the detonation wave regime (number and direction of waves) and the detonation wave structure, image processing procedures were applied. These routines are described in the following sections.

2.6.1. Detonation Wave Regime (SA-Z)

The image processing method used on the downstream high-speed camera is based on publications from Bennewitz et al. [11,12]. The implementation at DLR has already been described in detail in a previous publication from Bard et al. [24]. Here, only a summary of the most important steps is given.

In order to get a time-resolved evolution of the detonation waves, first the high-speed camera data is cut into segments of 500 frames each (equal to ≈2.8 ms). Next, an image correction is applied by removing the mean image and increasing contrast and brightness. The location of the chamber annulus is identified in a second step by performing a pixel-wise Fast Fourier Transformation (FFT) and identifying the pixels with the highest dynamics. The annulus is then divided into 360 bins. The number of waves and their direction can finally be derived either from angular-time (θ-t) plots of the intensity or from a 2D-FFT [24]. Knowing the dominant frequency f, the outer diameter of the RDC d_c and the number of waves n_w, the wave speed u_w can be calculated directly by using the following equation:

$$u_w = \frac{f \pi d_c}{n_w}. \tag{1}$$

2.6.2. Detonation Wave Structure from OH* (SA-X2)

The detonation wave structure can be observed in the radial OH* high-speed images. First, the OH* images are post-processed to increase intensity, contrast and plotted in false color. Since rotating detonation waves are highly dynamic and to a certain extent, also chaotic, additional methods to gain more insights into the time-averaged wave structure are applied. In order to do so, a two-dimensional pixel-wise standard deviation is calculated. This standard-deviation map shows the locations of the strongest intensity dynamics. Thus, the standard deviations should give an indication of the location of the detonation waves.

In addition, a phase-averaging algorithm is applied to the data to calculate a mean detonation wave structure. The image sequence is analyzed using a structured processing workflow to extract the wave front characteristics. Initially, the images are pre-processed to adjust the brightness level. The following procedure is applied to test segments of 10,000 frames each. For that purpose, a mean horizontal gradient, aligned with the direction of the passing wave, is computed first using a moving window approach. This also serves to smooth the signal and reduce local fluctuations. The result is a one-dimensional signal indicating the passing wave position in the window region. An FFT is then applied to extract the main frequency component, its amplitude and the corresponding phase angle. To ensure that only images containing a wave are retained, the images are then filtered based on the amplitude strength. The remaining images are sorted into 120 bins according to their phase. A mean phase-averaged image is then computed for each bin, creating a sequence of images that can then be used for further analysis [22].

For the determination of the angles of the leading detonation wave and the oblique shock wave, each phase-averaged image is smoothed using a Gaussian blur to suppress surface noise caused by impurities in the quartz glass. A brightness threshold is then applied to identify the contour of the leading wave fronts. Two linear regressions are then fitted to this contour, separated by the inclination point of the wave front. Thus, two angles are obtained: one for the detonation wave front and one for the start of the oblique shock. These angles are calculated for each phase-averaged image to increase the statistics of the resulting angles and to evaluate the uncertainty.

In addition, a decomposition method was also applied to the high-speed imaging of OH* emission. The standard DMD algorithm assumes a linear system [42] and is, for that reason, not a well-fitting approach for the optical analysis of detonation waves, especially in the case of counter-rotating modes [25]. Therefore, a nonlinear DMD analysis decomposing the data into dynamics at certain frequencies can be achieved via a Koopman operator. The Koopman theory states that with a suitable transformation, each nonlinear system can be linearly mapped with the Koopman operator. However, except for canonical problems, it was not yet possible to describe nonlinear systems through an infinite-dimensional linear (Koopman) operator and corresponding nonlinear functions (observables) analytically. Recent studies approximated the Koopman operator via neural networks [43,44].

3. Results

As was described before, three hot-fire tests were conducted with the quartz ring installed. Figure 7 shows the RDC with optical access during one of the hot-fire tests. It can also be observed in Figure 7 that part of an O-ring overlaps with the downstream side of the optical access windows. This part of the overlayed O-ring was forgotten to be removed during the assembly, but has no impact on the operation of the RDC. This is later also the case in the OH* high-speed imaging of the waves. However, the O-Ring covers less than the last 2 mm of the window and the most important area of injection and where the detonation waves can be expected, is not covered by the O-ring.

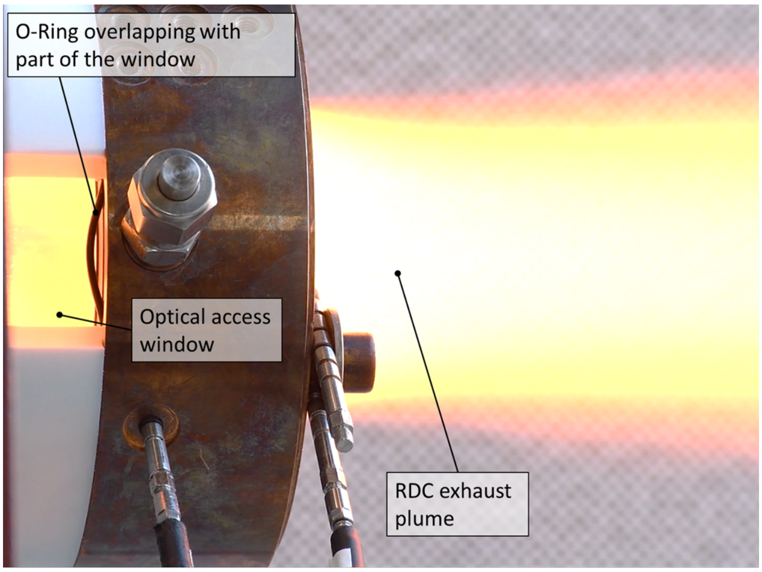

Figure 7. DLR RDC setup with optical access window during a hot-fire test [22].

3.1. Detonation Wave Regime

Figure 8 shows a snapshot of the post-processed downstream high-speed camera data with the mean image removed and in false color. Three regions with high intensity can be seen in the image, which would indicate a three-wave mode case [22].

However, from past RDC test analysis, it is known that the wave mode can change rapidly during a test, and the information from single snapshots can be misleading. Thus, Figure 9 now shows the wave mode analysis for the whole duration of one of the two similar test runs. The plot shows wave speed over time for several short-duration intervals, which are individually processed. The color of the scatter points indicates spinning in a clockwise or counterclockwise direction. If the algorithm detected counter-rotating modes, this is highlighted by the smaller black dots within the larger scatter plots.

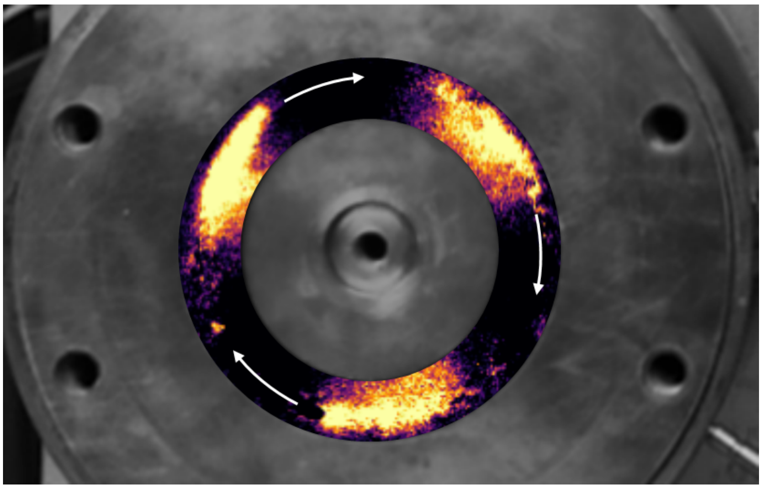

Figure 8. Visualization of the waves inside the annular detonation chamber through the back-end high-speed camera (SA-Z) during one of the test runs with optical access.

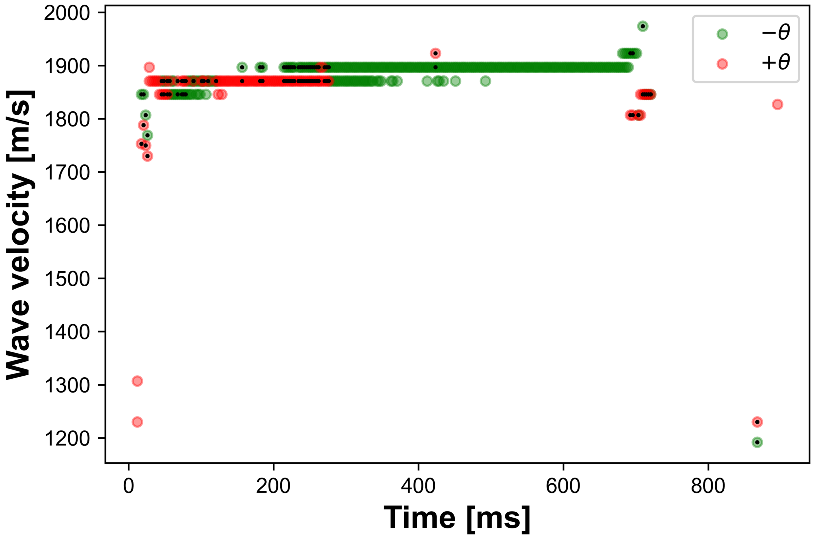

Figure 9. Detonation wave characteristics (velocity and direction) over the duration of one of the optical test runs. Black dots indicate counter-rotating waves [22].

From the given plot, it can be seen that during the start-up transient up until about 300 ms the system is quite chaotic with an increasing number of waves due to increasing mass flow rates, followed by a period of counter-rotating waves. However, from about 300 ms to 650 ms a relatively stable co-rotating wave regime establishes. This regime is characterized by three co-rotating waves with a wave speed of 1900 m/s [22]. The general behavior showed high reproducibility, since in the other test run, also three stable co-rotating waves appeared for a similar period of the test run and with a wave speed of 1880 m/s. Due to the slightly different ROF (see Table 2) in both tests, the relative wave speed is 71% of the CJ-velocity. Only for very short durations, weaker counter-rotating waves were observed, which quickly decayed and disappeared. This was also observable in the OH* imaging through the optical access window.

Figure 10 now shows the θ-Time plot of the enrolled intensity of the central line of the RDC annulus for a short period of the analyzed larger time window between 300 to 600 ms. The three co-rotating waves can clearly be seen by the parallel lines with three intersections with an imaginary vertical line at a specific time.

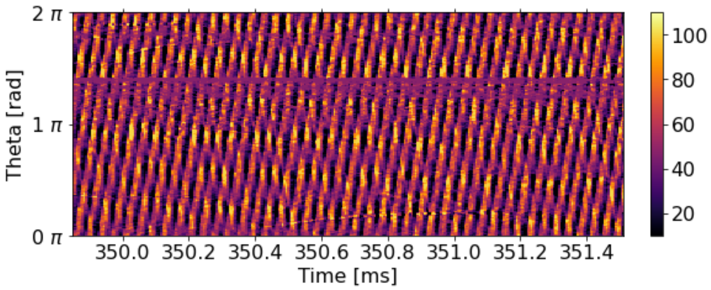

Figure 10. θ-Time plot indicating the detonation wave regime of three waves [22].

3.2. OH* Imaging of the Detonation Wave Structure

Now the OH* images from the radially placed high-speed camera are investigated. Figure 11 shows two snapshots of the OH* imaging. Here, the bulk flow is in an upward direction, and thus the injection plane would be on the lower side of the images.

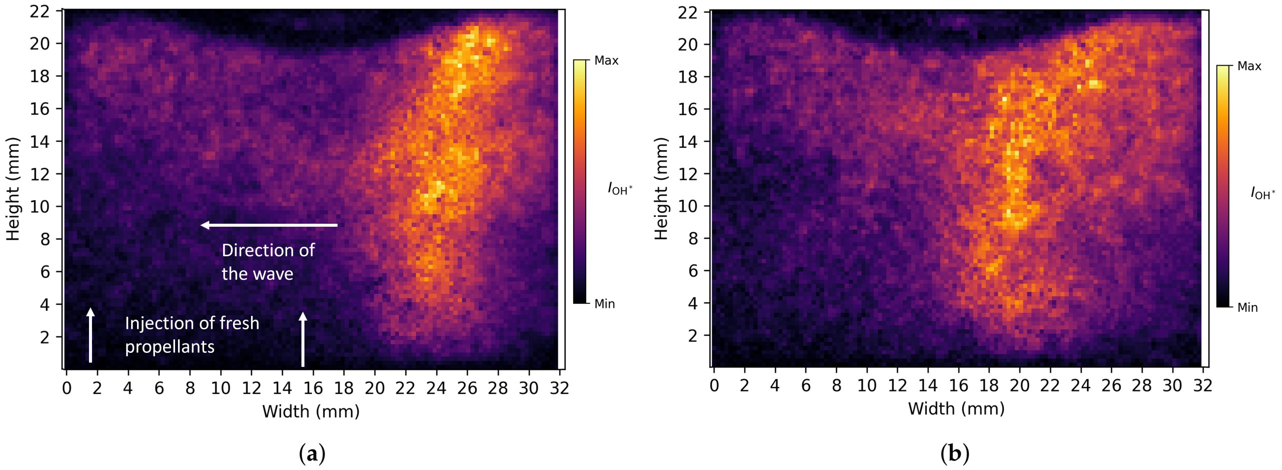

Figure 11. Snapshots of the OH* imaging of two consecutive waves passing by the optical access window. (**a**) at t_1 = 350 ms. (**b**) Next wave at $t_2 = t_1 + 38.9$ µs.

Taking into account the slightly different radial position of the waves in the two snapshots with the additional information that there are three co-rotating waves, the wave speed can also be calculated using the radial position and the number of frames between the two images and yields 1930 ± 60 m/s. The wave speed is therefore consistent with the one calculated from the visualization of the waves from the back-end high-speed camera.

Even though the OH* images have a low signal-to-noise ratio due to the low intensity at these shutter speeds, a thin region of high intensity, which is traveling through the field of view of the window, is clearly visible. By looking at the time evolution of the snapshots, it is also clear that the wave propagates from right to left. By counting the pixels with the highest intensity in radial direction at different axial positions and using the Millimeter to pixel conversion of the field of view of the optical access, it can be calculated that in the radial direction, the thin high OH* intensity region stretches between approximately 2 to 4 mm. Similar to previous work on RDEs [6], the observed characteristic dimensions of the detonation waves are also presented in non-dimensional form by normalizing with the detonation cell size λ. Since it is not feasible to accurately measure the detonation cell size inside the rotating detonation chamber, which depends on several parameters, which vary strongly in space and time, such as the temperature, pressure and composition of the gas in-front of the detonation wave, the theoretical or ideal cell size assuming a gas composition in-front of the wave, which consists purely of the perfectly mixed fresh ly injected propellants, is taken into account. Assuming a detonation cell size λ of 1.7 mm for the given operating conditions, the reaction zone of the detonation wave would therefore have a thickness of approximately 1–2 λ.

At the location of the detonation wave, the intensity increases in the axial direction. First, there is a region of relatively low OH* emissions starting from the injection plane at 0 mm up until about 3 mm. Caused by the close proximity ot the injection plane, it can be assumed that the mixture quality of the fresh gases is rather low in that zone. After this darker zone, the intensity then increases in the axial direction until the maximum values are reached at about 10 mm from the injection plane. Furthermore, in front of the detonation wave, a dark zone of lower intensity at the bottom of the chamber between 0 and about 10 mm can be observed. This indicates the injected fresh gas mixture of hydrogen and oxygen, which forms a triangle between two consecutive waves. There are also large regions of medium OH* intensity; for example, behind the detonation wave and axially downstream of the darker zone, indicating the fresh gas mixture. These medium intensity zones show, to a certain extent, the combustion products from the previous waves and also parasitic deflagration of where unburnt hydrogen and oxygen.

As can be seen in Figure 11, the detonation wave has a slightly different structure in each recorded frame. Thus, in order to gain a better understanding of the time-averaged structure of the detonation wave inside the RDC, the pixel-wise standard deviation of the intensity oscillations, as well as phase-averaging, was applied to a sample of 10,000 snapshots of the high-speed camera. Figure 12 shows the calculated 2D standard deviation of the OH* intensity. The highest dynamics can be seen at the height of 10–15 mm.

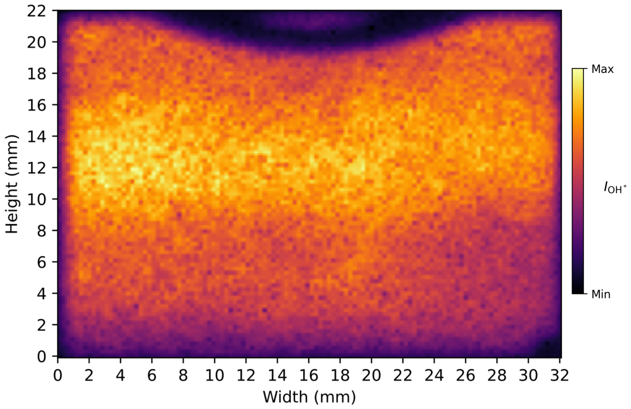

Figure 12. Standard deviation of each pixel averaged over 10,000 frames.

Since the RDC should ideally be rotationally symmetric, a line plot of the radially averaged standard deviation in dependence on the window height is presented in Figure 13. The main observation remains the same: the highest intensity oscillations are present between 10 and 15 mm downstream of the injection plane. The main observation from Figures 12 and 13 is that the highest standard-deviation of the oH* intensity appears between 10 and 15 mm, which was surprising, because a rather continuously high standard deviation over the full axial extent of the detonation was expected. Taking into account the fill height correlation from Bykovskii et al. [6], a height h of 20 ± 8 mm can be calculated, and thus it was expected that there is a strong intensity oscillation with an almost constant standard deviation in axial extent until the end of the detonation waves, where the standard deviation should reduce sharply. This sharp drop can clearly be observed in Figure 13 starting at 14 mm. This can be interpreted as a more statistical indication of the detonation wave height in this case. However, why the standard deviation is relatively low from a height of 0 to 10 mm and why there is an intermediate plateau of the standard deviation between 3 and 8 mm was not expected and is currently also not fully understood.

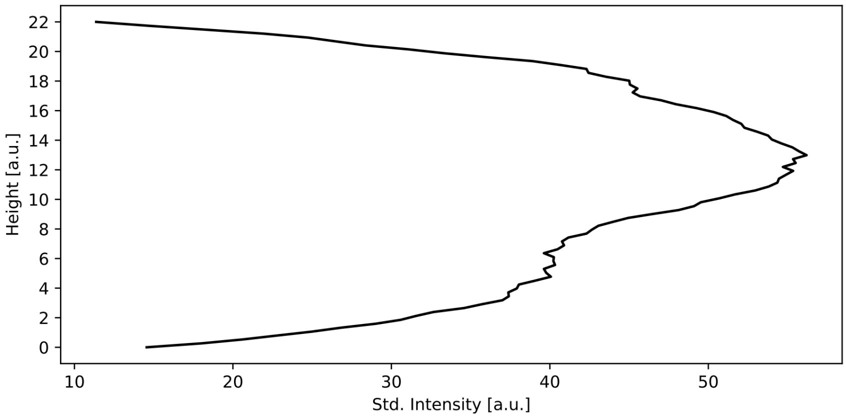

Figure 13. Radially averaged standard deviation of the intensity variation plotted over the axial height of the window.

With the nonlinear Koopman network decomposition, the rotating detonation wave frequency could clearly be identified. The KoopNet mode of the detonation wave was then combined with the mean image to reconstruct the detonation wave structure. Caused by the nonlinearity, each reconstructed image shows a different detonation wave structure. Figure 14 shows two exemplary reconstructed images of the detonation wave mode. The wave direction is again from right to left as in the original unprocessed high-speed images (see Figure 11). However, for the sake of completeness, the wave direction is again indicated with an arrow. The thin high-intensity regions can clearly be identified. Furthermore, OH* emissions behind this thin zone can be observed, which could indicate deflagration of propellants behind the detonation wave. The area before the waves only shows low OH* emission.

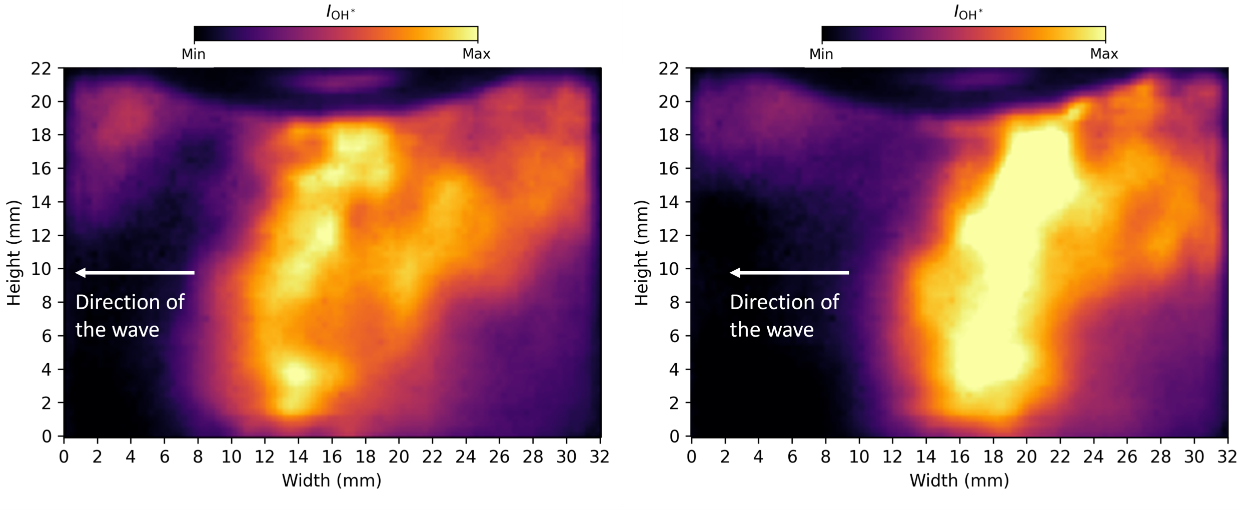

(**a**) (**b**)

Figure 14. Exemplary images of the reconstructed KoopNet mode of the detonation wave (**a**) at exemplary time 1 and (**b**) at exemplary time 2.

To get a clearer impression of the actual time-averaged structure of the rotating detonation waves an phase-averaged image of the detonation wave is calculated and presented in Figure 15. Between 0 and 12 mm, there is a slight forward leaning angle and starting at 14 mm until the downstream end of the window, the angle turns backwards. The point of inflection is located at about 11 to 12 mm.

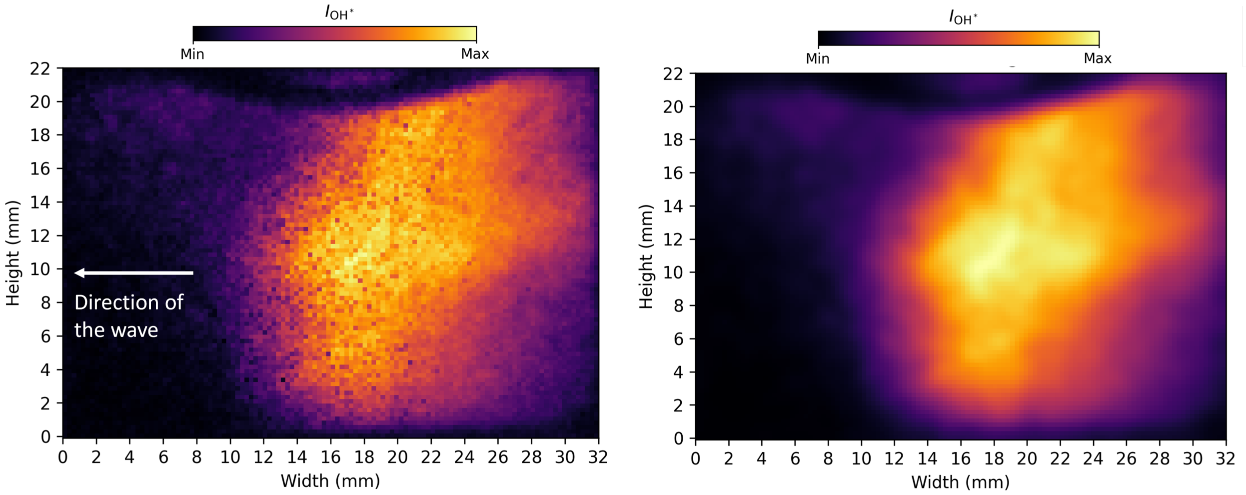

(**a**) (**b**)

Figure 15. Phase-averaged OH* images of the wave. (**a**) Original. (**b**) Smoothed.

In order to better visualize the structure of the wave, an edge detection algorithm was applied to the smoothed phase-averaged image to identify the wave front. The result of this analysis is presented in Figure 16. In addition, linear regressions were fitted to the upper and lower parts of the edge detection to approximate the forward and backward leaning angles of the detonation and the shock wave.

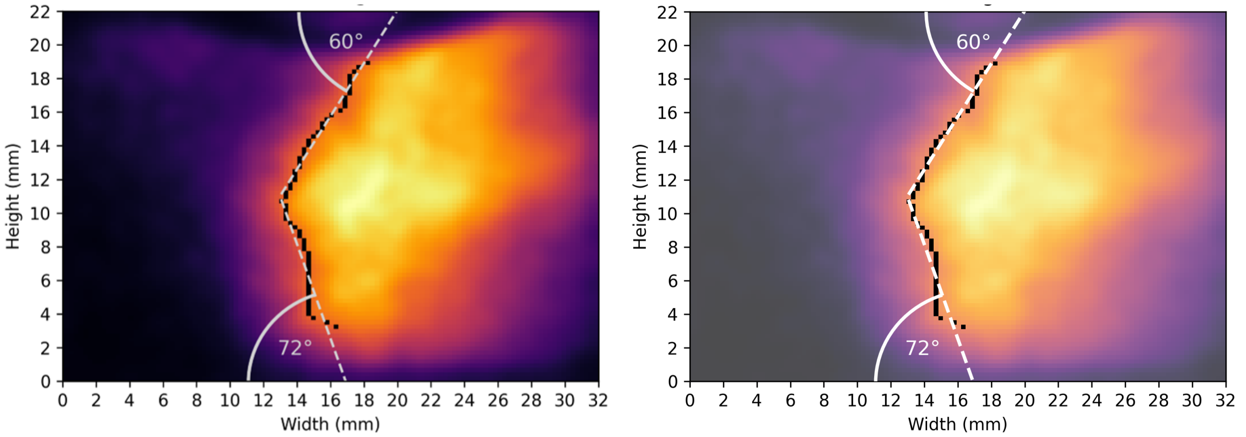

(**a**) (**b**)

Figure 16. Phase-averaged OH* image of the wave with applied edge detection for the wave front. (**a**) smoothed phase-averaged image from Figure 15 (**b**) increased brightness of background for better visibility of the edge detection curve and the fitted lines.

4. Discussion

Assuming that the point of inflection in the wave images is a marker for the detonation wave height, the detonation wave height for these conditions would be around 11 mm or $(7 \pm 1\ )\lambda$, which lies at the lower end of the well-known correlation by Bykovskii et al. [6]. Here, h is the mixing height of the fresh propellants, which is typically in the order of the detonation height or slightly larger [28]. However, compared to the correlation from Bykovskii et al., the wave height in this hydrogen–oxygen RDC has a lower uncertainty and also the actual height for this experiment is clearly at the lower end of the $h \approx (12 \pm 5)\lambda$ range. Due to the now more precise range of the detonation wave height for these conditions, improved injector designs, which are optimized to fill only the first 8λ of the detonation channel instead of up to 17λ can be derived and tested in future work.

However, why both the standard deviation and the phase-averaged images show the highest intensity at an axial distance of 9–14 mm downstream of the injection plane and not over the full height of the detonation wave, which theoretically should extend from close to the injection plane until the h is currently not fully understood. A possible explanation could be that in the short time frame in between two consecutive waves, the best fresh gas mixture quality is achieved in the location of 8–15 mm downstream of the injection plane and thus the rotating detonation waves show the strongest chemical reactions in this region. More insights into this axial evolution of the OH* intensity oscillations could be obtained from CFD modeling of the given combustor and operating condition. Numerical studies of this RDC are currently ongoing and first simulation results have recently been published [45]. Even though different operating conditions were modeled, the CFD indicated that 3D effects of the larger 10 mm gap size compared to the previously tested 4.5 mm gap size stabilize the detonation waves in the DLR combustor. In addition, the results also predicted the best fresh propellant mixing and the most intense detonation waves to be observed at around 4 and 10 mm downstream of the injection plane, which very well agrees with the experimental observations in this study. However, a similar simulation of the exact experimental setup and operating condition of the optical access RDC tests of this study needs to be performed in order to confirm that the observations from Bard et al. [45] are similar for these conditions and to gain a better understanding of the injection, propellant mixing and wave stabilization for the given condition.

In the circumferential direction of the channel, the high intensity region in the phase-averaged images extends between 4 and 8 mm. This would correlate with 2 to 5 λ and is significantly larger than expected widths of the reaction zone of detonation waves, which is usually less than λ [6,46]. However, in the single snapshots presented in Figure 11, the high intensity region and thus the combustion zone of the detonation wave appear much thinner. Here, the thickness of the high-intensity zone appears to be about 1–4 mm thick, which would be around (1–2.4) λ. This shows that the phase-averaging routine contributes to the thickening of the high-intensity region in the radial direction. Most likely, this is due to the challenging resolution of the phase bins, due to the high wave speed and the small window. An additional effect, which could explain the slightly increased extension of the detonation wave width compared to what is expected from literature, is due to the curvature of the channel and the relatively large annular gap width of 10 mm. The structure of detonation waves in curved channels has been investigated by several studies [47,48], and it was found that the detonation wave front in curved channels is not planar but gets bent. Due to the projection of the curved wave front onto the camera chip, this could also lead to a thickened detonation wave in the OH* imaging.

Figure 17 shows the detonation front of a hydrogen–oxygen detonation wave in a curved channel with an outer radius of $d = 120$ mm and a channel width of 20 mm [47]. It can be seen that the wave front is not a planar wave normal to the channel walls, but the curved channel bends the wave front itself. Now, assuming that in the studied RDC with an outer diameter of 68 mm and a channel width of 10 mm, a similar shape of the wave front is present, the line-of-sight projection, which is recorded by the camera chip, would lead to a thickening of the detonation wave front. A sketch of this described effect of the curved waves leading to a thickening in the visualization of the OH* emission of the wave front through the projection on the camera chip can be seen in Figure 18.

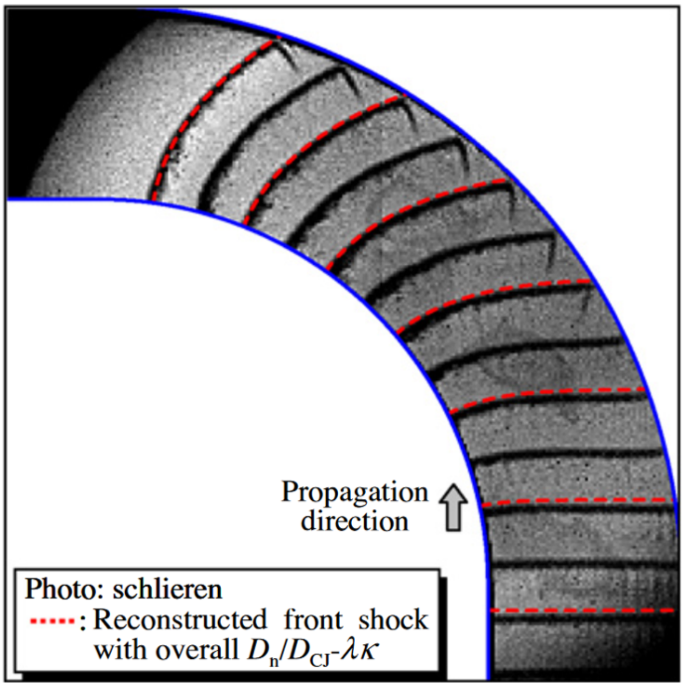

Figure 17. Hydrogen–oxygen detonation wave front in a curved channel [47].

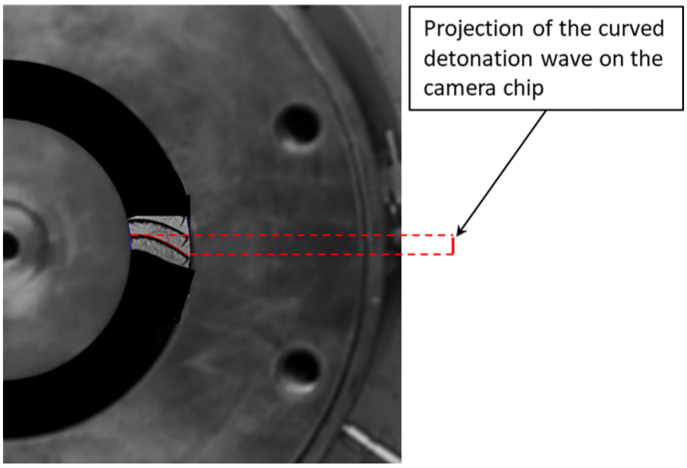

Figure 18. Detonation wave front in a curved channel from [47] overlayed on the RDC of this study. The Projection of the curved wave front on the radial camera chip, leading to a thickening of the reaction zone in radial direction, is indicated.

However, in the single snapshots presented in Figure 11, the high intensity region and thus the combustion zone of the detonation wave appears much thinner. Here, the thickness of the high-intensity zone appears to be t about 2–3 mm thick, which would be around 1–2 λ. This shows that most likely both the projection from the curved detonation wave and the phase-averaging routine contribute to the thickening of the detonation wave in Figures 15 and 16.

Now that the structure of the wave front is derived from the OH* imaging, this information can be combined with the additional geometrical information of the chamber annulus and the number of waves to create a sketch of the hydrogen–oxygen detonation wave structure in the DLR RDC for the given operating conditions. This simplified model is presented in Figure 19. Here, h is the filling height of the fresh gases in front of the detonation wave, h_w the height of the detonation wave itself, and l the distance between two consecutive waves. Based on the imaging, three main angles can be defined: α is the angle of the detonation wave front with respect to the injection plane, β is the angle of the start of the oblique shock wave and δ is the angle of the triangle of the fresh gas mixture.

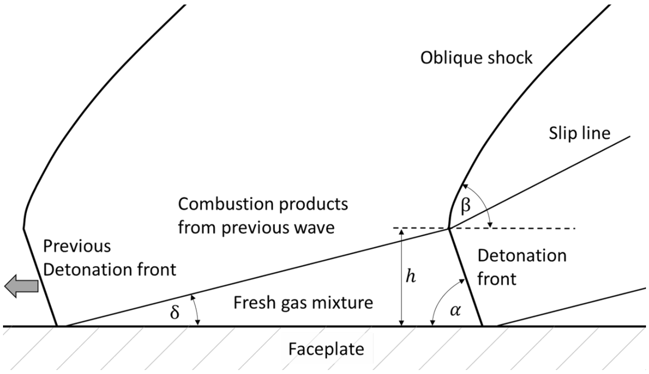

Figure 19. Sketch of the dimensions and features of a detonation wave in an RDC. Modified from [10].

The final geometrical features of the detonation wave structure can be described as follows. The height of the fresh gas mixture h is estimated to be about 12 mm from the injection plane. The detonation wave height h_w is about 11 mm or 6–8 detonation cell seizes λ. Knowing that three co-rotating waves are present in the chamber, the distance l between two consecutive waves can be calculated and is 70 mm. Thus, the angle of the boundary between the injected fresh gas mixture and the burnt products from the previous wave is estimated with $\delta = 10°$. As was explained before, the angles of the detonation wave and the oblique shock wave are both obtained from the fitting of linear regressions to the edge detection wave front in the phase-averaged images. Since, for each bin, a different phase-averaged image, including slightly different angles are processed, the mean angles from all phase-averaged images are calculated. The forward leaning angle of the detonation wave is $\alpha = 74 \pm 4°$. The trailing oblique shock starts at the inflection point located 12 mm from the injection plane. If an angle of a linear approximation is fitted to the first few millimeters of the curved shock, the angle of this line can be approximated with $\beta \approx 61 \pm 3°$. Finally, in Figure 20, these geometrical characteristics are now overlayed on the phase-averaged, smoothed OH* imaging [22].

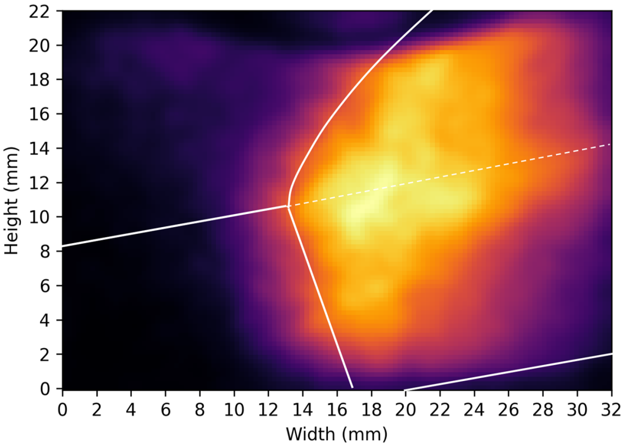

Figure 20. Phased-averaged OH* image with the overlayed extracted wave features [22]. The white lines represent the features shown in Figure 19, such as the detonation wave front, the oblique shock wave and the boundary between the fresh injected propellants and the combustion products from the previous wave. The white dashed line indicates another prominent feature in the OH* images, which could be the slip line.

5. Summary & Conclusions

In Rotating Detonation Combustors, the injector design is crucial for obtaining stable detonation waves. However, in order to design these injectors, it is important to have an understanding of the required filling height of the fresh gas mixture that is consumed by one detonation wave. However, the well-known semi-empirical correlation to estimate this filling height from Bykovskii et al. [6] has an uncertainty of ±33%. For that reason, radial optical access is a powerful diagnostic method in order to increase the understanding of the interaction of the injection and mixing of fresh propellants and the detonation waves in RDCs. For that reason, radial visualization of the detonation wave structure was already applied in several studies. However, to the author's knowledge up to today, there exists only one previous publication including radial visualization of hydrogen–oxygen detonation waves in rotating detonation rocket combustors by Bykovskii et al. [20]. But in this experiment, important information, such as the injector geometry, is not well documented. For that reason, an optical access quartz ring was integrated into an existing RDC at DLR. Two tests with similar steady-state operating conditions were analyzed. During these tests, the wave dynamics showed good repeatability, and in both tests, there were longer durations with stable co-rotating cases of three waves. The wave speed was about 1900 m/s or 71% of the theoretical CJ-velocity.

A second high-speed camera was placed normal to the RDC axis and captured OH* emissions with 180,000 FPS through a quartz window that covered approximately 22 mm in axial direction of the detonation chamber and about 30 mm in circumferential direction, which translates to an angular field of view of 31° of the annular chamber.

The OH* images clearly showed the passing waves in the field of view. The post-processing of the images indicates that the mixing height of the fresh propellants for the investigated conditions is about 11 mm and therefore about (6–8)λ from the injection plane. Furthermore, the OH* intensity was also low between 0 mm and up to about 2–3 mm from the injection plane, which shows that the good mixing of the fresh propellants seems to be present between 3 mm and 12 mm, and thus the waves are not traveling directly on the faceplate but slightly lifted. A phase-averaged image was calculated to show the structure of the passing detonation wave. An edge-detection algorithm was applied to the phase-averaged image and revealed a forward-leaning detonation wave with an angle of $74 \pm 4^\circ$. At a distance of 10–12 mm from the injection plane, there is an inflection point and a backward-leaning edge in OH* intensity that can be observed. This is currently interpreted as the start of the oblique shock.

The presented visualization of the detonation wave structure will be useful for the design of new injectors for future hydrogen–oxygen RDCs at DLR, since the filling height is now characterized. Based on the presented findings, new injectors with adjusted injection velocities for this wave height will be designed and tested in future work. Furthermore, in order to better understand the influence of injectors and the mixing quality on the wave dynamics, the optical access and the processing methods of this study could be applied to new injector designs and other operating conditions. In addition, the results could also be valuable for the validation of CFD simulations, because, to the authors' knowledge, this study presents the first visualization of the hydrogen–oxygen detonation wave structure in a well-documented RDC experiment.

Author Contributions: Conceptualization, W.A. and E.B.; methodology, E.B., J.M. and K.R.; software, K.R. and J.M.; formal analysis, W.A. and K.R.; investigation, E.B., W.A., M.B., L.L. and S.G.; resources, M.B., J.S.H. and S.G.; data curation, S.G. and W.A.; writing—original draft preparation, W.A., J.M. and E.B.; writing—review and editing, W.A., J.S.H., M.B. and E.B.; visualization, L.L. and S.G.; supervision, W.A., M.B. and J.S.H.; project administration, J.S.H.; funding acquisition, J.S.H. All authors have read and agreed to the published version of the manuscript.

Funding: This research received no external funding.

Data Availability Statement: The original contributions presented in this study are included in the article. Further inquiries can be directed to the corresponding author.

Acknowledgments: The numerical support and feedback on the experimental results from colleagues at ONERA was useful for the design of the experiment and is greatly acknowledged. Additional thanks to the test bench technicians and mechanics for setting up the experiment.

Conflicts of Interest: The authors declare no conflicts of interest.

References

1. Heister, S.D.; Smallwood, J.; Harroun, A.; Dille, K.; Martinez, A.; Ballyntin, N. Rotating Detonation Combustion for Advanced Liquid Propellant Space Engines. *Aerospace* **2022**, *9*, 581. [CrossRef]
2. Wolański, P. Detonative Propulsion. *Proc. Combust. Inst.* **2013**, *34*, 125–158. [CrossRef]
3. Ma, J.Z.; Luan, M.; Xia, Z.; Wang, J.; Zhang, S.; Yao, S.; Wang, B. Recent Progress, Development Trends, and Consideration of Continuous Detonation Engines. *AIAA J.* **2020**, *58*, 4976–5035. [CrossRef]
4. Voitsekhovskii, B.V. Maintained Detonations. *Sov. Phys. Dokl.* **1960**, *4*, 1207.
5. Nicholls, J.A.; Cullen, R.E.; Ragland, K.W. Feasibility studies of a rotating detonation wave rocket motor. *J. Spacecr. Rocket.* **1966**, *3*, 893–898. [CrossRef]
6. Bykovskii, F.A.; Zhdan, S.A.; Vedernikov, E.F. Continuous Spin Detonations. *J. Propuls. Power* **2006**, *22*, 1204–1216. [CrossRef]
7. Frolov, S.M.; Aksenov, V.S.; Ivanov, V.S.; Medvedev, S.N.; Shamshin, I.O.; Yakovlev, N.N.; Kostenko, I.I. Rocket Engine with Continuous Detonation Combustion of the Natural Gas–Oxygen Propellant System. *Dokl. Phys. Chem.* **2018**, *478*, 31–34. [CrossRef]
8. Davidenko, D.M.; Gökalp, I.; Kudryavtsev, A.N. Numerical simulation of the continuous rotating hydrogen-oxygen detonation with a detailed chemical mechanism. In Proceedings of the West-East High Speed Flow Field Conference, Moscow, Russia, 19–22 November 2007.
9. Wang, R.B.; Webb, A.M.; Camacho, R.D.; Slipchenko, M.; Braun, J.; Meyer, T.R.; Athmanathan, V.; Fugger, C.A.; Roy, S.; Perkins, H.D. Characterization of reactant refill and detonation wave dynamics in a Natural Gas/GOx rotating detonation engine using simultaneous high repetition-rate OH-PLIF and chemiluminescence. In Proceedings of the AIAA SciTech 2024 Forum, Orlando, FL, USA, 8–12 January 2024.
10. Michalski, Q.; Aliakbari, R.; Mason-Smith, N.; Paull, N.; Wenzel, M.; Pudsey, A. Structure of rotating detonation in mixtures of natural gas and oxygen. *Combust. Flame* **2024**, *260*, 113253. [CrossRef]
11. Bennewitz, J.W.; Bigler, B.R.; Hargus, W.A.; Danczyk, S.A.; Smith, R.D. Characterization of detonation wave propagation in a rotating detonation rocket engine using direct high-speed imaging. In Proceedings of the 2018 Joint Propulsion Conference, Cincinnati, OH, USA, 9–11 July 2018.
12. Bennewitz, J.; Bigler, B.; Schumaker, S.; Hargus, W.J. Automated image processing method to quantify rotating detonation wave behavior. *Rev. Sci. Instrum.* **2019**, *90*, 065106. [CrossRef]
13. Bennewitz, J.W.; Bigler, B.R.; Ross, M.C.; Danczyk, S.A.; Hargus, W.A.; Smith, R.D. Performance of a Rotating Detonation Rocket Engine with Various Convergent Nozzles and Chamber Lengths. *Energies* **2021**, *14*, 2037. [CrossRef]
14. Hellard, P.; Gaillard, T.; Davidenko, D.; Berterretche, P.; Zitoun, R.; Vidal, P. Quasi-CJ rotating detonation with partially premixed methane-oxygen injection: Numerical simulation and experimental validation. *Appl. Energy Combust. Sci.* **2024**, *19*, 100278. [CrossRef]
15. Teasley, T.W.; Fedotowsky, T.M.; Gradl, P.R.; Austin, B.L.; Heister, S.D. Current State of NASA Continuously Rotating Detonation Cycle Engine Development. In Proceedings of the AIAA SciTech 2023 Forum, National Harbor, MD, USA, 23–27 January 2023.
16. Stechmann, D.P. Experimental Study of High-Pressure Rotating Detonation Combustion in Rocket Environments. Ph.D. Thesis, Purdue University, West Lafayette, IN, USA, 2017.
17. Bohon, M.D.; Bluemner, R.; Paschereit, C.O.; Gutmark, E.J. High-speed imaging of wave modes in an RDC. *Exp. Therm. Fluid Sci.* **2019**, *102*, 28–37. [CrossRef]
18. Rankin, B.A.; Fotia, M.L.; Naples, A.G.; Stevens, C.A.; Hoke, J.L.; Kaemmming, T.A.; Theuerkauf, S.W.; Schauer, F.R. Overview of Performance, Application, and Analysis of Rotating Detonation Engine Technologies. *J. Propuls. Power* **2017**, *33*, 131–143. [CrossRef]
19. Frolov, S.M.; Aksenov, V.S.; Ivanov, V.S. Experimental proof of Zel'dovich cycle efficiency gain over cycle with constant pressure combustion for hydrogen–oxygen fuel mixture. *Int. J. Hydrogen Energy* **2015**, *40*, 6970–6975. [CrossRef]
20. Bykovskii, F.A.; Zhdan, S.A.;Vedernikov, E.F. Continous Spin Detonation of Hydrogen-Oxygen Mixtures. 1. Annular Cylindrical Combustors. *Combust. Explos. Shock Waves* **2008**, *44*, 150–162. [CrossRef]

21. Sosa, J.; Burke, R.; Ahmed, K.A.; Micka, D.J.; Bennewitz, J.W.; Danczyk, S.A.; Paulson, E.J.; Hargus, W.A. Experimental evidence of H_2/O_2 propellants powered rotating detonation waves. *Combust. Flame* **2020**, *214*, 136–138. [CrossRef]
22. Armbruster, W.; Bard, E.; Börner, M.; Rheindorf, K.; Lober, L.; General, S.; Hardi, J. Visualization of the Detonation Wave Structure in a Small-Scale Hydrogen-Oxygen Rotating Detonation Combustor. In Proceedings of the 35th International Symposium on Space Technology and Science (ISTS), Tokushima, Japan, 12–18 July 2025.
23. Bykovskii, F.A.; Zhdan, S.A.; Vedernikov, E.F. Realization and Modeling of Continuous Spin Detonation of a Hydrogen-Oxygen Mixture in Flow-Type Combustors. *Combust. Explos. Shock Waves* **2009**, *45*, 716–728. [CrossRef]
24. Bard, E.; Armbruster, W.; Rheindorf, K.; Bee, A.; Börner, M.; General, S.; Hardi, J.; Davidenko, D.; Boulal, S.; Vidal, P. Experimental Study of a Subscale Rotating Detonation Chamber Fed with GH2/GO2. In Proceedings of the 9th Space Propulsion Conference, Glasgow, UK, 20–23 May 2024.
25. Armbruster, W.; Börner, M.; Bee, A.; Martin, J.; Knapp, B.; General, S.; Hardi, J.S.; Bard, E. Experimental Investigation of a Small-Scale Oxygen-Hydrogen Rotating Detonation Rocket Combustor. In Proceedings of the AIAA SciTech 2024 Forum, Orlando, FL, USA, 8–12 January 2024.
26. Peng, H.-Y.; Liu, W.-D.; Liu, S.-J.; Zhang, H.-L.; Jiang, L.-X. Flowfield Analysis and Reconstruction of Ethylene–Air Continuous Rotating Detonation Wave. *AIAA J.* **2020**, *58*, 5036–5045. [CrossRef]
27. Wang, R.B.; Suppiah, A.; Braun, J.; Fugger, C.A.; Roy, S.; Perkins, H.D.; Paniagua, G.; Athmanathan, V.; Meyer, T.R. Characterization of an optically accessible RP/GOx rotating detonation engine. In Proceedings of the AIAA SciTech 2024 Forum, Orlando, FL, USA, 8–12 January 2024.
28. Rankin, B.A.; Codoni, J.R.; Kevin Y.C.; Hoke, J.L.; Schauer, F.R. Investigation of the structure of detonation waves in a non-premixed hydrogen–air rotating detonation engine using mid-infrared imaging. *Proc. Combust. Inst.* **2019**, *37*, 3479–3486. [CrossRef]
29. Aliakbari, R.; Michalski, Q.; Maseon-Smith, N.; Pudsey, A.; Wenzel, M.; Paull, N. Heat Flux Measurements of a Methane-Oxygen Rotating Detonation Rocket Engine. In Proceedings of the International Workshop on Detonation for Propulsion, Berlin, Germany, 15–19 August 2022.
30. Athmanathan, V.; Braun, J.; Ayers, Z.; Fisher, J.M.; Fugger, C.A.; Roy, S.; Paniagua, G.; Meyer, T.R. Detonation structure evolution in an optically-accessible non-premixed H_2-Air RDC using MHz rate imaging. In Proceedings of the AIAA SciTech 2020 Forum, Orlando, FL, USA, 6–10 January 2020.
31. Ishihara, K.; Yoneyama, K.; Sato, T.; Watanabe, H.; Itouyama, N.; Kawasaki, A.; Matsuoka, K.; Kasahara, J.; Matsuo, A.; Funaki, I. Visualization and Performance Evaluation of a Liquid-Ethanol Cylindrical Rotating Detonation Combustor. *Trans. Jpn. Soc. Aeronaut. Space Sci.* **2023**, *66*, 46–58. [CrossRef]
32. Nakata, K.; Ishihara, K.; Goto, K.; Iouyama, N.; Watanabe, H.; Kawasaki, A.; Matsuoka, K.; Kasahara, J.; Matuso, A.; Funaki, I.; et al. Experimental investigation of inner flow of a throatless diverging rotating detonation engine. *Proc. Combust. Inst.* **2023**, *39*, 3073–3082. [CrossRef]
33. Fan, W.J.; Peng, H.Y.; Liu, S.J.; Sun, M.B.; Yuan, X.Q.; Zhang, H.L.; Liu, W. Initiation process of non-premixed continuous rotating detonation wave through Schlieren visualization. *Combust. Flame* **2024**, *265*, 113437. [CrossRef]
34. Armbruster, W.; Hermannsson, B.S.; Börner, M.; Bee, A.; Martin, J.; Hardi, J. Experimental Investigation of a Small-Scale Oxygen-Hydrogen Rotating Detonation Combustor. In Proceedings of the 34th International Symposium on Space Technology and Science, Kurume, Japan, 3–9 June 2023.
35. Börner, M.; Bee, A.; Traudt, T.; Klein, S.; Hardi, J. Overview of the DLR M3 Test Field for Component Testing for Cryogenic Propulsion. In Proceedings of the 3rd Global Business Services Forum 2022, Marseille, France, 6–8 December 2022.
36. Bard, E.; Armbruster, W.; General, S.; Knapp, B.; Bee, A.; Börner, M.; Manassis, K.; Strauss, F.; Hardi, J.S.; Davidenko, D.; et al. Investigation of the Influence of Operation and Injection Conditions on the Wave Dynamics in GH2/GO2 RDCs. In Proceedings of the 35th International Symposium on Space Technology and Science, Tokushima, Japan, 12–18 July 2025.
37. Ditsche, F.; Petersen, J.; Propst, M.; Armbruster, W.; Börner, M.; Hardi, J.; Tajmar, M.; Bach, C. Heat Flux Measurements in a small-scale Oxygen-Hydrogen Rotating Detonation Rocket Combustor. In Proceedings of the 35th International Symposium on Space Technology and Science, Tokushima, Japan, 12–18 July 2025.
38. Armbruster, W.; Bard, E.; Boulal, S.; Börner, M.; General, S.; Bee, A.; Hardi, J.S. Design and testing of a hydrogen–oxygen pre-detonator for rotating detonation engines. *CEAS Space J.* **2025**, *17*, 969–979. [CrossRef]
39. Walter, I.V.; Journell, C.L.; Lemcherfi, A.; Gejji, R.M.; Heister, S.D.; Slabaugh, C.D. Operability of a natural gas–air rotating detonation engine. *J. Propuls. Power* **2020**, *36*, 453–464. [CrossRef]
40. Kaneshige, M.; Shepherd, J.E. *Detonation Database, Explosion Dynamics Laboratory Report FM97-8*; California Institute of Technology: Pasadena, CA, USA, 1999.
41. Gordon, S. McBride, B.J. *Computer Program for Calculation of Complex Chemical Equilibrium Compositions and Applications*; Part 1: Analysis; NASA Glenn Research Center: Cleveland, OH, USA, 1994.
42. Schmid, P.J. Dynamic Mode Decomposition of Numerical and Experimental Data. *J. Fluid Mech.* **2010**, *656*, 5–28. [CrossRef]

43. Omi, K.; Nakayama, K.; Hirose, K.; Takizawa, K.; Tagushi, H.; Nakaya, S.; Tsue, M. Nonlinear mode decomposition of combustion instabilities under various jet-to-crossflow momentum ratios in a hydrogen-rich ram combustor using a deep Koopman network. *Combust. Flame* **2024**, *268*, 113643. [CrossRef]
44. Martin, J.; Nakaya, S.; Börner, M.; Hardi, J. Nonlinear mode decomposition of unsteady LOX/LNG flame imaging in an optically accessible rocket combustor. In Proceedings of the 35th International Symposium on Space Technology and Science, Tokushima, Japan, 12–18 July 2025.
45. Bard, E.; Davidenko, D.; Boulal, S.; Vidal, P.; Armbruster, W.; Börner, M.; Hardi, J. Experimental and CFD Study of a Sub-scale Rotating Detonation Combustor fed with Gaseous H_2-O_2. In Proceedings of the 4th HiSST, Tours, France, 22–26 September 2025.
46. Austin, J.M.; Pintgen, F.; Shepherd, J.E. Reaction zones in highly unstable detonations. *Proc. Combust. Inst.* **2005**, *30*, 1849–1857. [CrossRef]
47. Nakayama, H.; Kasahara, J.; Matsuo, A.; Funaki, I. Front shock behavior of stable curved detonation waves in rectangular-cross-section curved channels. *Proc. Combust. Inst.* **2013**, *34*, 1939–1947. [CrossRef]
48. Melguizo-Gavilanes, J.; Rodriguez, V.; Vidal, P.; Zitoun, R. Dynamics of detonation transmission and propagation in a curved chamber: A numerical and experimental analysis. *Combust. Flame* **2021**, *223*, 460–473. [CrossRef]